PHYSICS

Correlated oxide Dirac semimetal in the extreme quantum limit

Jong Mok Ok[1†‡], Narayan Mohanta[1†], Jie Zhang[1†], Sangmoon Yoon[1], Satoshi Okamoto[1], Eun Sang Choi[2], Hua Zhou[3], Megan Briggeman[4,5], Patrick Irvin[4,5], Andrew R. Lupini[1], Yun-Yi Pai[1], Elizabeth Skoropata[1], Changhee Sohn[1], Haoxiang Li[1], Hu Miao[1], Benjamin Lawrie[1], Woo Seok Choi[6], Gyula Eres[1], Jeremy Levy[4,5], Ho Nyung Lee[1]*

Quantum materials (QMs) with strong correlation and nontrivial topology are indispensable to next-generation information and computing technologies. Exploitation of topological band structure is an ideal starting point to realize correlated topological QMs. Here, we report that strain-induced symmetry modification in correlated oxide $SrNbO_3$ thin films creates an emerging topological band structure. Dirac electrons in strained $SrNbO_3$ films reveal ultrahigh mobility ($\mu_{max} \approx 100{,}000\ cm^2/Vs$), exceptionally small effective mass ($m^* \sim 0.04m_e$), and nonzero Berry phase. Strained $SrNbO_3$ films reach the extreme quantum limit, exhibiting a sign of fractional occupation of Landau levels and giant mass enhancement. Our results suggest that symmetry-modified $SrNbO_3$ is a rare example of correlated oxide Dirac semimetals, in which strong correlation of Dirac electrons leads to the realization of a novel correlated topological QM.

INTRODUCTION

Gaining control over the properties of quantum correlation and topology in quantum materials (QMs) is a critical step in advancing the physics of QMs that can promote innovation in many technological areas (*1*–*3*), such as spintronics and quantum technologies. Therefore, the discovery of QMs in which both quantum correlation and topology are achieved is a subject of current interest. Quantum spin liquids (*4*–*6*), topological superconductors (*7*, *8*), quantum anomalous Hall materials (*9*, *10*), and fractional quantum Hall systems (*11*–*16*) are good examples of correlated topological QMs whose properties depend on both correlation and topology. Moreover, strongly correlated materials highlighting many-body interactions are good examples of material systems to study entanglement. Thus, creating and understanding entangled states in QMs are important steps toward quantum technologies. One way to achieve entangled states in solids is to reach the extreme quantum limit (XQL) (*12*, *15*–*17*) (i.e., all carriers occupying entirely the lowest Landau level) at which correlations between charge carriers are maximized (*18*, *19*). At the XQL, the strong correlation gives rise to fractional quasiparticles, and some of them are expected to obey nonabelian statistics (*20*, *21*). The latter element is one of the most basic requirements for topological quantum computing.

Chalcogenide- and halogen-based materials have been at the center of the development of topological QMs (*1*–*3*, *22*–*24*) because of their topological band structure and large spin-orbit coupling (SOC). However, the weak correlation in these topological materials hinders the appearance of key emergent phenomena, such as magnetism and superconductivity. Thus, the co-design approach, i.e., adding correlation to these topological materials, is currently under active investigation (*22*–*24*). A conventional approach includes both doping with 3*d* magnetic elements with strong correlation and creating heterostructures with magnetic and/or superconducting materials (*7*, *9*, *10*, *22*–*24*). Such an approach, however, is a formidable task presenting a number of technical challenges.

In this context, transition metal oxides (TMOs) provide a versatile platform, owing to their inherent strong electron correlation and SOC (*25*, *26*), as well as advancements in their thin-film synthesis and device fabrication. However, challenges also remain in studying TMOs, as the discovery of topological band structures is limited to only a couple of (or few) materials (*27*–*30*). Among oxide materials, 4*d* TMOs could be promising candidates, as they offer a good balance between electron correlation and SOC. Recently, a theoretical study predicted a topological band structure in an orthorhombic phase with $a^-a^-c^+$ octahedral rotations in $SrNbO_3$ (*31*). Dirac points in $SrNbO_3$, however, were predicted to exist far from the Fermi level. Although the electronic structure of perovskite oxides can be modified through the strain control of octahedral rotations (*32*, *33*), the viability of creating a novel Dirac semimetal with strained $SrNbO_3$ by manipulating the octahedral rotations has not been explored.

RESULTS

To experimentally realize the Dirac semimetallic state theoretically predicted in the 4*d* perovskite $SrNbO_3$ (*31*), an accurate determination of the crystallographic symmetry and its deliberate control are important. The utilization of epitaxial strain is known to be an effective method to modify the symmetry near the interface in a heterostructure (*32*, *33*). Although the crystallographic details of the perovskite $SrNbO_3$ have not been widely studied because of the difficulty of synthesizing the stoichiometric perovskite phase, a recent study with a polycrystal reported the lattice parameters of $a = \sqrt{2}a_p = 5.6894$ Å, $b = \sqrt{2}a_p = 5.6944$ Å, and $c = 2a_p = 8.0684$ Å ($\alpha = \beta = \gamma = 90°$) with an orthorhombic structure (space group: *Pnma*) (*34*). With a pseudocubic approximation, the lattice parameter *a* is

[1]Oak Ridge National Laboratory, Oak Ridge, TN 37831, USA [2]National High Magnetic Field Laboratory, Florida State University, Tallahassee, FL 32310, USA. [3]Advanced Photon Source, Argonne National Laboratory, Lemont, IL 60439, USA. [4]Department of Physics and Astronomy, University of Pittsburgh, Pittsburgh, PA 15260, USA. [5]Pittsburgh Quantum Institute, Pittsburgh, PA 15260, USA. [6]Department of Physics, Sungkyunkwan University, Suwon 16419, Korea.
*Corresponding author. Email: hnlee@ornl.gov
†These authors contributed equally to this work.
‡Present address: Department of Physics, Pusan National University, Busan 46241, Korea.

4.023 Å (*34*, *35*). In this work, we grew $SrNbO_3$ films on lattice-mismatched $SrTiO_3$ substrates [a_s = 3.905 Å; therefore, the lattice mismatch of ε(%) = −3.02%] to induce epitaxial strain. To investigate the role of strain and the associated evolution of crystallographic symmetry, we systematically varied the thicknesses of films (d = 2.4 to 130 nm).

Epitaxial $SrNbO_3$ thin films were grown on (001) $SrTiO_3$ substrates by pulsed laser epitaxy. Despite the large lattice mismatch, high-quality $SrNbO_3$ thin films were successfully prepared, as was confirmed by several different methods, including reflection high-energy electron diffraction (RHEED), atomic force microscopy (AFM), x-ray diffraction (XRD), and cross-section scanning transmission electron microscopy (STEM) (see figs. S1 and S2). The films revealed sharp interfaces without any detectable interfacial intermixing. In addition, the films were fully strained up to d_{c1} = 7 nm and partially strained from d_{c1} to d_{c2} = 18 nm. We observed that the NbO_6 octahedra were collectively distorted and rotated by the compressive strain. The fully strained film exhibited pronounced c^- rotation-induced half-order peaks at (3/2 1/2 L/2), whereas these were absent in the fully relaxed thin films (Fig. 1C) (also see fig. S3). The relaxed films ($d > d_{c2}$) exhibited a bulk-like cubic structure with an $a^0a^0c^0$ symmetry without any oxygen octahedral rotations (OORs; Fig. 1A), whereas the fully strained films ($d < d_{c1}$) showed a tetragonal structure with $a^0a^0c^-$-type octahedral rotations (Fig. 1B). The octahedral distortions found in strained thin films significantly affected the electronic structure of this material. In the cubic $SrNbO_3$, there is no Dirac-like degeneracy (Fig. 1D), but the fourfold degeneracy remains intact at two high-symmetry points, P and N, in tetragonal $SrNbO_3$ with the $a^0a^0c^-$ symmetry. Nonsymmorphic symmetry, i.e., screw rotation along the z direction, is known to protect the degeneracy at these two high-symmetrical points (see figs. S4 and S5) (*36*).

To investigate how epitaxial strain affects the transport properties of $SrNbO_3$ thin films, we first measured the temperature-dependent resistivity (T = 2 to 300 K) at different thicknesses and zero magnetic field (Fig. 2A). Our films (d = 2.4 to 27.2 nm) exhibit clear metallic behavior down to 2.4 nm in thickness. A gradual reduction in the overall resistivity is observed as the thin-film samples become partially strained at around the second critical thickness d_{c2} (Fig. 2B). In addition, the resistivity drastically increases at the ultrathin limit below d_{c1} (Fig. 2, A and B). The change in resistivity is attributed to a significant reduction in the carrier density (Fig. 2C and figs. S6 and S7), supporting a strain-induced electronic structure modification in $SrNbO_3$ ultrathin films, as expected from density functional theory (DFT) calculations. Note that such a huge change in carrier density is unusual, but it is reminiscent of topological materials, in which two to three order-of-magnitude changes in the carrier density have been reported when a transition from the topological phase to the correlated phase (e.g., superconductivity) occurred (*37*, *38*). On the other hand, the resistivity of the relaxed films was around ~80 μΩ·cm at room temperature, which is of the same order of magnitude as a $SrNbO_3$ film grown on a $KTaO_3$ substrate with a smaller lattice mismatch (ε ~ −0.85%) (*34*). These results strongly suggest that the observed transport properties are intrinsic to $SrNbO_3$, ruling out a possible contribution from oxygen vacancies in $SrTiO_3$ substrates (see fig. S2).

Having established that transport behaviors were the intrinsic properties of $SrNbO_3$ thin films, we measured the Hall effect of our films with a wider range of film thickness (d = 2.4 to 74 nm) to further understand the strain effect on the electronic state. As shown in fig. S6, three different types of Hall effects are observed when the thickness is varied. Fully relaxed films ($d > d_{c2}$) show a linear Hall effect, from which we extracted the carrier density ($n = 1/|e| \cdot dB/d\rho_{xy}$) and mobility ($\mu = (|e|\rho_{xx}n)^{-1}$). The carrier densities of the relaxed films

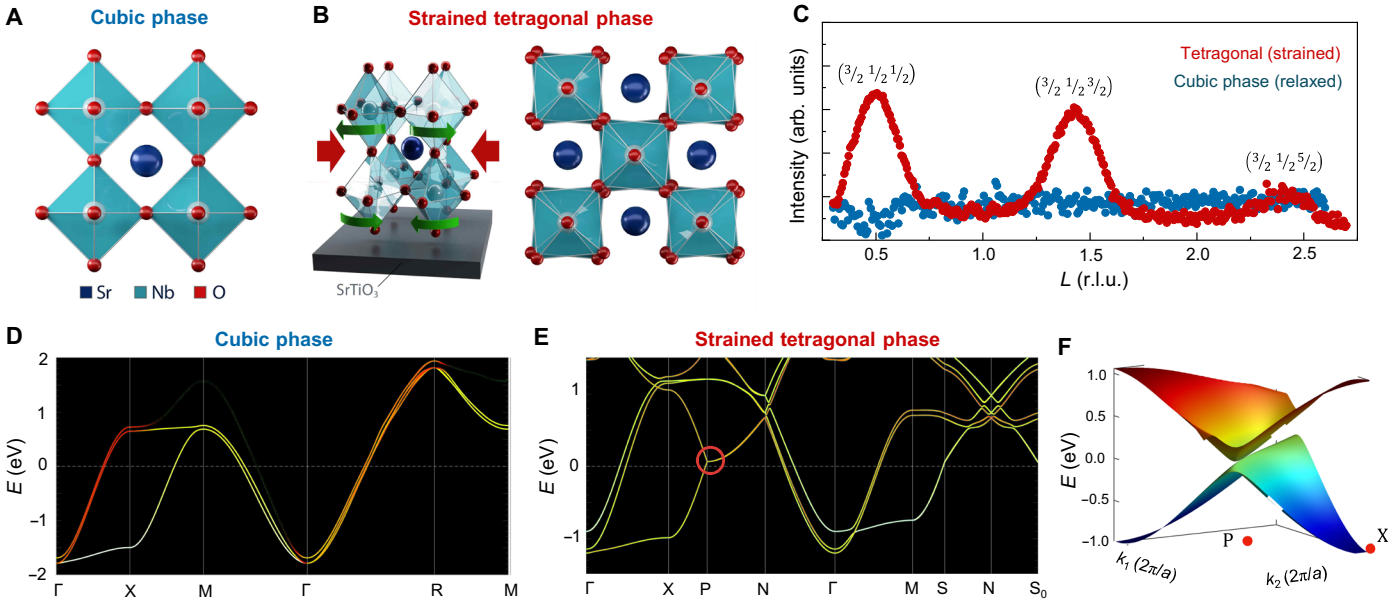

Fig. 1. Strain-induced Dirac metallic state in $SrNbO_3$ thin films. (**A** and **B**) Octahedral distortion pattern for (A) cubic $SrNbO_3$ ($a^0a^0a^0$ in the Glazer notation) and (B) strained tetragonal $SrNbO_3$ ($a^0a^0c^-$). Epitaxial strain induces octahedral distortion. (**C**) Octahedral rotation-induced half-order superstructure diffraction peaks of (3/2 1/2 L/2) with L = 1, 3, 5 for fully strained (red, 7.2 nm, c^- rotation) and fully relaxed (blue, 130 nm, c^0 rotation) $SrNbO_3$ thin films. r.l.u., reciprocal lattice unit. (**D** and **E**) Calculated electronic structure of (D) cubic $SrNbO_3$ and (E) strained tetragonal $SrNbO_3$. The red circle in plot (E) shows the Dirac point that appears near the Fermi level at the P point in the strained tetragonal phase. (**F**) Dirac dispersions near the P point within the tetragonal Brillouin zone. The larger Fermi velocity in the tetragonal phase, near the P point, would lead to higher carrier mobility and a favorable source of a nontrivial Berry phase in the presence of a magnetic field.

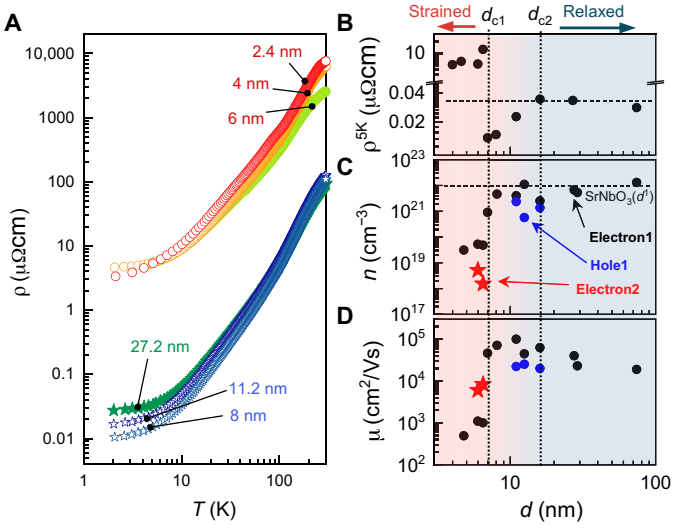

Fig. 2. Thickness dependence of electronic state of $SrNbO_3$ thin film. (**A**) Temperature dependence of resistivity of $SrNbO_3$ thin films with various thicknesses of 2.4 to 27.2 nm. (**B** to **D**) Thickness dependence of (B) resistivity, (C) carrier density, and (D) mobility of $SrNbO_3$ thin films at 2 K. The carrier density of a relaxed thin film is well explained by the d^1 electron configuration. An additional electron carrier, which has high mobility $\mu \approx 10{,}000$ cm^2/Vs but extremely small carrier density $n \approx 1.5 \times 10^{18}$ cm^{-3}, is observed in the strained thin films. The additional electron band has an experimentally reachable quantum limit of $H^*_{QL} \sim 3.3$ T because of its extremely small carrier density.

were $n \approx 1.29 \times 10^{22}$ cm^{-3}, consistent with both the calculated value from a d^1 electron configuration of $n^{theory} \approx 1.53 \times 10^{22}$ cm^{-3} and the values of the $SrNbO_3/KTaO_3$ samples mentioned previously (*34*). The mobility of the relaxed films was $\mu \approx 10$ $cm^2/V{\cdot}s$ at 300 K, which was again in good agreement with the $SrNbO_3/KTaO_3$ samples (*34*). The low-temperature mobility of our samples, however, was 100 times higher than that of the $SrNbO_3/KTaO_3$ samples because of the huge dielectric screening of $SrTiO_3$ at low temperature (*39*). Unlike the relaxed films, the strained samples ($d < d_{c2}$) exhibited nonlinear Hall effects. The nonlinear Hall effects can be explained with a two-carrier model by introducing an additional carrier (*40*), which presumably arises from the Dirac dispersion. The thickness-dependent carrier density and mobility are summarized in Fig. 2 (C and D). Note that the highest mobility observed is $\mu^{max} \approx 100{,}000$ $cm^2/V{\cdot}s$. This mobility value is higher than that of a correlated Dirac semimetal $CaIrO_3$ single crystal (*27*) and $SrTiO_3$ single crystals (*41*). The mobility of $SrNbO_3/SrTiO_3$ is 10 times higher than that of bulk $SrTiO_3$-related materials ($\mu^{STO} \sim 10{,}000$ $cm^2/V{\cdot}s$) because of the effective mass difference ($m^{STO}/m^{SNO} \sim 10$), which is described below.

The additional small carriers evolve from holes into electrons as a function of thickness (Fig. 2C). Below 7 nm, the additional electron carrier has an extremely small carrier density of $n \approx 1.5 \times 10^{18}$ cm^{-3} and a high mobility of $\mu \approx 10{,}000$ $cm^2/V{\cdot}s$. When the threefold valley and spin degeneracy are considered, the small electron carrier corresponds to a Fermi surface size of $S_F \approx 3.15 \times 10^{-4}$ $Å^{-2}$, of which the quantum limit is $H^*_{QL} \sim 3.3$ T. Thus, these carriers under this XQL offer an opportunity to study the strongly interacting topological electrons and their entangled states. Also, note that the magnetic field required to reach the quantum limit in strained $SrNbO_3$ is only ~3.3 T, which is immensely lower than that for any conventional conducting oxides ($H^*_{QL} \sim 10^5$ T) (*42*).

To further investigate the quantum limit of a strained $SrNbO_3$ thin film (d = 6.4 nm), we studied magnetotransport properties at 0.15 to 10 K up to 30 T. To check the reproducibility of our results, four different samples (named S1 to S4) were investigated (see fig. S8). All samples show clear quantum oscillations with qualitatively similar behaviors. First, we rotated the direction of the applied magnetic field with respect to the [001] axis and measured the quantum oscillations at several different angles (θ = 0 to 90°) (Fig. 3A). The quantum oscillations become more apparent in their second derivatives ($-d^2\rho/dH^2$) (Fig. 3B). The quantum oscillations survive at higher angles and do not exhibit 1/cosθ scaling; this behavior is attributed to the three-dimensional (3D) characteristics of the Fermi surface. The 3D character of the Fermi surface provides independent evidence to support the hypothesis that the transport properties originated from $SrNbO_3$ itself rather than from the interface with $SrTiO_3$ (see the Supplementary Materials for detailed discussions). The first evidence to support the quantum limit of $SrNbO_3$ thin films is an unsaturated linear magnetoresistance (MR) (Fig. 3C). At lower magnetic fields, the MR shows conventional H^2 behavior, but it changes to a linear MR at $H^*_{QL} \sim 3.3$ T or higher. There are various possible mechanisms for this behavior. However, we attribute the unsaturated linear MR in the strained $SrNbO_3$ to quantum-linear MR (*43*) because it has a low carrier density. This unsaturated linear MR is a characteristic of Dirac/Weyl semimetals at the quantum limit, as has been reported for many Dirac/Weyl semimetals (*44*–*46*).

Another important piece of evidence of the quantum limit was found in quantum oscillations. Conventional quantum oscillations for higher Landau levels are periodic in inverse magnetic fields (1/H). However, the quantum oscillations recorded for strained $SrNbO_3$ films exhibit an intriguing aperiodic behavior (Fig. 4, A and B). This anomaly in the quantum oscillations provides an important characteristic unique to strained $SrNbO_3$ films. We attribute this quantum transport anomaly to the fractional occupation of the Landau levels owing to the strong correlation. As illustrated in fig. S9, we found that the Landau fan diagram (1/H versus N) deviates significantly from the linear dependence when it is plotted by assigning the minima of resistivity—i.e., the second derivative of ρ_{xx} ($-d^2\rho/dH^2$)—to integer numbers (N). When $\rho_{xy} >> \rho_{xx}$ in a $SrNbO_3$ thin film is considered, the minima of ρ_{xx} can be assigned to N because $\sigma_{xx} = \rho_{xx}/(\rho_{xx}^2 + \rho_{xy}^2) \sim A\rho_{xx}$, where A is a prefactor. Such a strong deviation is obviously different from conventional quantum oscillations, even considering Zeeman splitting. On the other hand, the Landau fan diagram exhibits a clear linear relationship when the minima of the quantum oscillations are assigned to the rational fractions of the Landau integers N = 1/3, 2/3, 4/3, 5/3, 2/5, 3/5, 4/5, 3/7, 4/7, 5/7, 6/7, and 4/9 (Fig. 4, A and B) (also see fig. S9). To ensure the reproducibility of this intriguing phenomenon, we tested four different samples, and it was observed persistently in all the samples (see Fig. 4C and figs. S8 and S9). We further note that while the origin is still under debate, similar aperiodic quantum oscillations were reported in the 3D topological semimetal $ZrTe_5$ (*16*, *17*).

DISCUSSION

The entire series of fractional numbers of Landau integers seen in our strained perovskite oxide is highly extraordinary, as only extremely clean systems, including graphene (*11*) and GaAs-based 2D electron gases (2DEGs) (*12*), have revealed such a complete set of fractional states. Only a portion of the fractional numbers have been

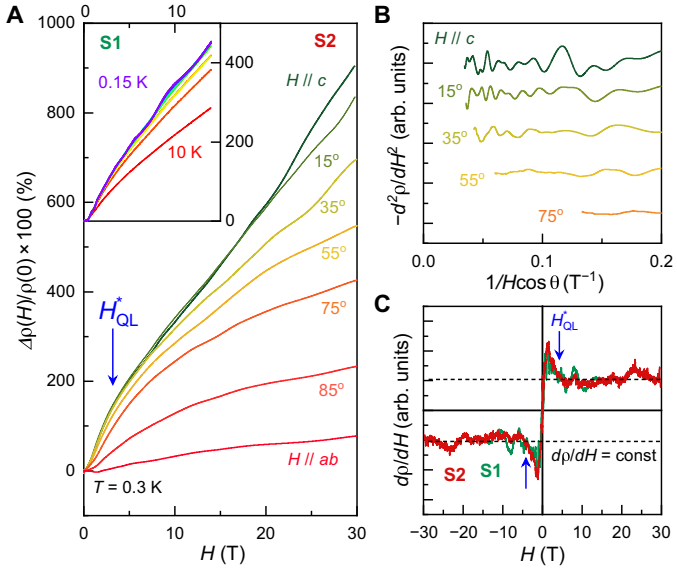

Fig. 3. Angular dependence of quantum oscillations. (**A**) MR for different angles up to 30 T at 0.3 K. Inset shows MR for different temperatures (T = 0.15 to 10 K). Quantum oscillations and linear MR are clearly observed in $SrNbO_3$. (**B**) Second derivative of resistivity ($-d^2\rho/dH^2$) for different angles. Quantum oscillations are observed for all different angles and do not follow the 1/cosθ behavior, supporting the 3D character of the Fermi surface. (**C**) First derivative of resistivity ($d\rho/dH$) for two different samples at 0.3 K. The linear MR starts to develop at H^*_{QL} ~ 3.3 T.

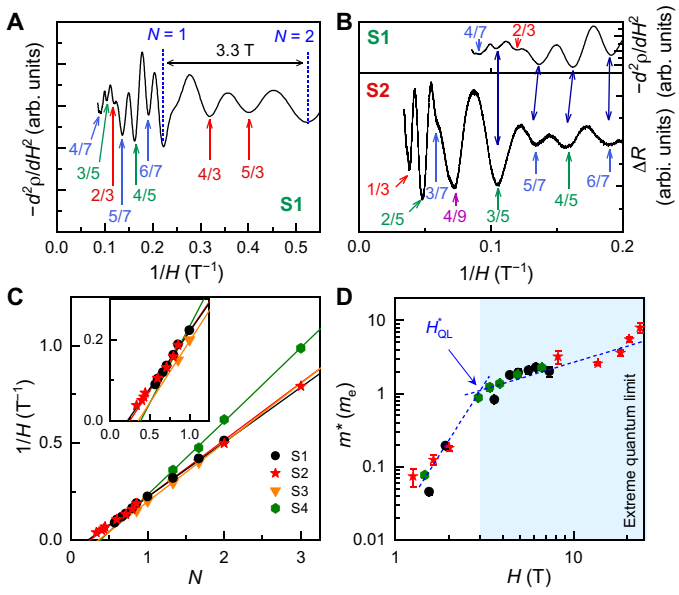

Fig. 4. Anomalous quantum oscillations in the quantum limit. (**A**) $-d^2\rho/dH^2$ as a function of 1/H under a magnetic field of up to 14 T for S1. The resistivity minima are assigned as integer (fractional) Landau levels, as indicated by the arrows. (**B**) ΔR as a function of 1/H under a magnetic field of up to 30 T for S2. S1 and S2 samples show consistent behavior. (**C**) Landau fan diagram of the Landau level index N versus 1/H for four different samples. All samples show linear behavior. The inset shows an enlarged view of the high-field region. All samples have a nontrivial Berry phase as predicted by the calculations. (**D**) Effective mass at different magnetic fields for four different samples. Strong mass enhancement is found at H^*_{QL} ~ 3.3 T.

observed in previously reported 2D systems at the quantum limit, such as a silicon quantum well (*13*), MnZnO/ZnO (*14*), and the surface state of Bi_2Se_3 (*15*). We attribute the observation of the complete set of the factional Landau levels from the highly strained $SrNbO_3$ ultrathin films to their high mobility and strong correlation.

In addition, from the Landau fan diagram (Fig. 4C), we were able to determine the Fermi surface size S_F and Berry phase φ_B from the Lifshitz-Onsager quantization rule $S_F(\hbar/eH) = 2\pi(n + 1/2\text{-}\varphi_B/2\pi + \delta)$, where $\delta = 0$ for 2D or $\delta = \pm 1/8$ for 3D. On the basis of this rule, we estimated the Fermi surface size, $S_F \sim 3.3 \pm 0.2$ T $\approx (3.15 \pm 0.19) \times 10^{-4}$ Å^{-2}, which was in good agreement with the Hall data. Moreover, the Landau fan diagram confirms a nonzero Berry phase, as was predicted from the DFT calculations. The intercept of the Landau fan diagram was $(\varphi_B/2\pi + \delta) = 0.26 \pm 0.01$. Note that it is possible that the nonzero Berry phase originated from the surface Rashba bands of $SrTiO_3$, as recently observed in ultrathin $LaTiO_3/SrTiO_3$ (3 to 4 unit cells) heterostructures (*47*, *48*). However, that is unlikely to be the case in $SrNbO_3/SrTiO_3$, because $SrNbO_3$ is metallic, and the Fermi level lies well above the Rashba-type band crossing. Instead, the nonzero Berry phase observed in the $SrNbO_3$ thin film suggests that the 4*d* electrons in $SrNbO_3$, orbiting in cyclotron motion while enclosing a Dirac point in *k*-space, interacted strongly with one another and consequently formed fractional occupation of Landau levels. Thus, the aperiodic quantum oscillations and nontrivial Berry phase observed are unique for strained $SrNbO_3$ at the XQL compared with other oxide materials reported so far (see table S2).

The most interesting experimental finding arising from the strongly interacting electrons was temperature-dependent quantum oscillations. From the temperature-dependent quantum oscillations, the cyclotron mass m^* can be extracted, based on the Lifshitz-Kosevich formula $\Delta\rho_{xx} \propto (\alpha m^* T/H)/\sinh(\alpha m^* T/H)$, where $\alpha = 2\pi^2 ck_B \approx 14.69$ T/K.

The temperature-dependent quantum oscillations depended highly on the applied magnetic fields (see fig. S10). Although quantum oscillations at low magnetic fields can be observed clearly at up to ~7 K, those at high magnetic fields are suppressed quickly with increasing temperature. Figure 4D shows the magnetic field dependence of m^* for four different samples. At lower magnetic fields, below H^*_{QL} ~ 3.3 T, the effective mass is around $0.04m_e$—which is extremely light—as expected from the linear dispersion owing to the Dirac band of $SrNbO_3$ ($m^*_{DFT} \sim 0.026m_e$). We observed a sudden mass enhancement of up to ~$1m_e$ at H^*_{QL}. Beyond the quantum limit, m^* continuously increased to up to ~$10\ m_e$ at 30 T. Note that, although mass enhancement has been reported in GaAs (*49*), ZrTe (*16*), and ZrSiS (*50*), those systems showed only a miniscule increase in effective mass of ~200 to 300%.

Overall, these findings indicate that symmetry-modified $SrNbO_3$ is a 3D correlated oxide Dirac semimetal entering the XQL, in which topology meets many-body physics, yielding fractional occupation of Landau levels. Thus, we think that $SrNbO_3$ offers a promising platform for further exploration of exotic correlated quantum phases and behaviors that can provide innovative materials solutions for the next generation of quantum technologies.

MATERIALS AND METHODS

Film growth

Substrates of TiO_2-terminated $SrTiO_3$ (001) 5 × 5 mm^2 in size were prepared by etching with buffered hydrofluoric acid and annealing at 1000°C for 1 hour. A ceramic target was prepared by sintering mixtures of stoichiometric amounts of $SrCO_3$ and Nb_2O_5 powder at

1100°C for 10 hours, with an intermediate grinding and pelletizing step after the initial decarbonation step at 1000°C for 12 hours. A KrF excimer laser (λ = 248 nm) was used to ablate the target at a repetition rate of 5 Hz. $SrNbO_3$ thin films were grown on $SrTiO_3$ (001) substrates at optimum conditions of T_g = 650°C, $PO_2 < 4 \times 10^{-6}$ torr, and f = 0.4 J/cm^{-2}. Owing to the 5+ preference of the niobium valence, the perovskite phase (Nb^{4+}) is achieved only under precisely controlled conditions of oxygen pressure ($PO_2 < 10^{-5}$ torr) (*34*, *35*), similar to the conditions needed for $LaTiO_3$ (*51*, *52*).

Film thickness was calibrated by x-ray reflectivity using a four-circle diffractometer. Crystallinity and epitaxial strain were examined by XRD and reciprocal space mapping. The surface morphology measurements were made with an AFM (Veeco Dimension 3100). Figure S1A shows XRD patterns of the $SrNbO_3$ 002 peak at different thicknesses (d = 2.4 to 15.2 nm). We observed a clear peak position shift at the critical thickness of $d_{c1} \sim 7$ nm, which is consistent with the huge jump in low-temperature resistivity (see Fig. 2, A and B). Our thin films had atomically flat surfaces, as confirmed by the AFM image and the RHEED image shown in fig. S1 (B and C, respectively).

Charge accumulation at the interface from STEM-EELS analysis

Cross-sectional TEM specimens were prepared using low-energy ion milling at LN_2 temperature after mechanical polishing. High-angle annular dark field (HAADF) STEM measurements were performed on a Nion UltraSTEM200 microscope operated at 200 kV. The microscope was equipped with a cold field-emission gun and a corrector of third- and fifth-order aberrations for sub-angstrom resolution. A convergence half-angle of 30 mrad was used, and the collection inner and outer half-angles for HAADF STEM were 65 and 240 mrad, respectively. A collection aperture of 5 mm was used for electron energy loss spectroscopy (EELS) measurement, and EELS spectrum imaging was performed at a speed of 30 frames per second.

Figure S2A shows a HAADF STEM image of a $SrNbO_3$(d = 6.5 nm)/$SrTiO_3$ sample viewed along the [100] zone axis. The HAADF STEM image confirms that the $SrNbO_3$ thin film is epitaxially grown on the $SrTiO_3$ substrate with a sharp interface. Note that the nonuniform background contrast in the HAADF STEM image can be attributed to the amorphized surface of the TEM specimen, which was formed by argon ion milling. Figure S2 (B and C) shows the integrated Ti-$L_{2,3}$ and O-K edge EELS spectra across the interface. As shown in fig. S2B, the spectral features of the Ti-$L_{2,3}$ edge broaden with the approach from the substrate to the interface. Note that the spectral change is most prominent at the first unit cell of the substrate, and the EELS spectrum fully returns to the spectrum of standard $SrTiO_3$ from three unit cells below. This spectral change is attributed to the charge transfer from the $SrNbO_3$ thin film.

The broadening of theTi-$L_{2,3}$ edge spectra in $SrTiO_3$ could be due to any of the following three reasons (*53*): symmetry change at the interface, charge reduction due to oxygen vacancies, or charge reduction due to charge transfer from heteromaterials. On the basis of the HAADF STEM image, the first possibility can be ruled out because a sharp interface with a robust epitaxial relationship is observed. To further examine the origin of the charge reduction, we estimated the ratio between the titanium and oxygen continuum parts from the substrate bulk to the interface (fig. S2D). The continuum parts were used for the stoichiometry analysis because the near-edge structure was sensitive to the internal electronic states. As shown in fig. S2D, there was no significant difference between the interface and the substrate bulk. Rather, the ratio became higher at the interface layer of $SrTiO_3$, which can be attributed to the beam broadening (the signals from $SrNbO_3$ can additionally contribute to the O-K edge). The stoichiometry analysis suggested that the spectral change at the interface (1 unit cell of $SrTiO_3$) was mainly due to the charge transfer from the $SrNbO_3$ thin film.

In addition to the EELS results, there are several other pieces of evidence that the charge transfer from the $SrNbO_3$ thin film, not oxygen vacancies, induced the charge accumulation at the interface. During pulsed laser deposition, vacancies can be formed when high-energy plasma plumes collide with the substrate. Therefore, the formation of oxygen vacancies depends to a great extent on the growth conditions, mainly the oxygen pressure and laser fluence. Higher vacuum and laser fluence create more oxygen vacancies. Oxygen stoichiometric films, however, can be grown even in a high vacuum if the laser spot size and energy are optimized, as our group reported earlier (*54*). We used a laser with a low enough fluence (f = 0.4 J/cm^{-2}) to grow $SrNbO_3$ thin films. To check for a possible oxygen deficiency in the substrate, we grew $SrTiO_3$ film on a $SrTiO_3$ substrate in the same growth conditions used for the $SrNbO_3$ thin films. The $SrTiO_3$ thin films that were grown were totally insulating, supporting the hypothesis that interfacial charges are not related to oxygen deficiency. Thus, charge transfer was most likely the origin of interfacial electrons, as predicted by a theoretical study (*55*). Unlike oxygen vacancies, which can extend deep into the $SrTiO_3$ side (*56*), charge transfer is expected only at the interface (*57*) (maximum of 2 to 3 unit cells of $SrTiO_3$), which matches our observations well.

Lattice symmetry and strain-induced octahedral rotation of $SrNbO_3$

As shown in fig. S3 (A and B), we used x-ray Bragg rod diffraction L scans at four different H-K quadrants to check and determine the primary lattice symmetry of $SrNbO_3$ as a function of film thickness. We present the fully strained 7.2-nm and fully relaxed 130-nm films as representative results (we also similarly measured 1.8-, 16-, and 20-nm $SrNbO_3$ films). Both strained and relaxed $SrNbO_3$ films displayed fourfold rotational symmetry. The 7.2-nm film showed a tetragonal-like lattice symmetry ($c > a$) as a result of the compressive strain, whereas the 130-nm film revealed a cubic-like lattice symmetry ($c \approx a$).

OOR-induced perovskite lattice doubling produced a unique set of half-order superstructure Bragg peaks, which were used to determine the OOR pattern and quantify the rotation angles. For detailed OOR half-order peak investigations with very weak signals, we carried out synchrotron XRD measurements at room temperature at beamline 33-ID-D at the Advanced Photon Source at Argonne National Laboratory. Monochromatized x-rays with a wavelength of 0.61992 Å were used, and a Pilatus 100K photon-counting area detector was used to capture the weak half-order superstructure. To suppress the fluorescence signal of the $SrTiO_3$ substrate, higher-energy x-rays (E = 20 keV, well above the Sr K absorption edge) were chosen. Scattering geometric corrections and background subtractions using a photon-counting area detector were conducted for all films. We surveyed all possible types of OOR half-order peaks to determine the rotation pattern with Glazer notation. The total absence of (odd/2, even/2, odd/2), (odd/2, odd/2, even/2), and (odd/2, even/2, even/2) types of peaks ruled out the existence of in-phase (+) rotation along either the a or c lattice axis or the existence of perovskite A-site cation off-symmetry point displacement (not shown in fig. S3). As shown in fig. S3C, the (H/2 K/2 L/2) (H = K) type peaks are also

absent for all $SrNbO_3$ films with different thicknesses and strain states, which suggests that there is no a^- or b^- type in-plane, out-of-phase rotation for any of the $SrNbO_3$ films. As shown in fig. S3D, the (H/2 K/2 L/2) (H ≠ K) type peaks can be observed only in strained $SrNbO_3$ films (including a partially strained 16-nm film).

We then attempted to quantify the (H/2 K/2 L/2) (H ≠ K) type half-order Bragg rod to estimate the rotation amplitude (γ) for each strained film, using the scattering structural factor calculation of the complete heterostructure with a confined overall scale factor [via the diffraction intensity at the (002) thin-film peak]. In fig. S3E, the simulated OOR half-order Bragg rods with different rotation γ angles are compared with the measured data. Figure S3F displays the thickness dependence of extracted c^- octahedral rotation angle γ. More detailed information regarding the strain, symmetry, and octahedral rotation of $SrNbO_3$ thin films with different thicknesses is summarized in table S1. Both γ angles for 7.2- and 16-nm strained films are close to 10°, which was used for the DFT calculations. The ultrathin 1.8-nm film exhibits a relatively reduced γ angle, probably because of the proximity effect of octahedral connectivity imposed by the underlying $SrTiO_3$ substrate without any OOR ($a^0a^0a^0$).

Band structure calculation

First-principles electronic structure calculations were carried out within the framework of DFT on a plane wave basis with Perdew-Burke-Ernzerhof (PBE) exchange correlation (*58*), as implemented in the QUANTUM ESPRESSO simulation code (version 6.5) (*59*). We used a 7 × 7 × 8 Monkhorst-Pack *k*-point mesh to discretize the first Brillouin zone and a plane wave cutoff of 600 eV, which were found to be sufficient to achieve convergence of the total energy. The energy convergence criterion was set to 10^{-6} eV during the minimization process of the self-consistent cycle. Starting with the experimental lattice constants a = 5.518 Å, b = 5.518 Å, and c = 8.280 Å, full optimization of the $SrNbO_3$ tetragonal crystal structure (space group *I4/mcm* [140]) was performed using the force convergence criterion of 10^{-3} eV/Å. The calculations were performed with SOC both turned on and turned off.

The calculated Fermi surfaces of $SrNbO_3$ in the cubic (relaxed) and the tetragonal (strained) phases are shown in fig. S4. The three Fermi surfaces correspond to the three t_{2g} orbitals of niobium. The calculated band structure and Fermi surfaces of the cubic $SrNbO_3$ are consistent with recent reports (*60*, *61*). The heavier electronic band constitutes a larger Fermi surface in both the cubic and tetragonal phases. The Dirac point at the P point near the Fermi level in the tetragonal phase is visible in the Fermi surface (bottom left plot) in the form of a connection between two disjoint surfaces (small surface with blue top and bigger surface with yellow top) at the P point.

Because the Dirac point at the P point is closer to the Fermi level, it can act as a source of a nontrivial Berry phase in the presence of a magnetic field. On the other hand, the Dirac points at the N point appear at ~0.7 eV above the Fermi level. Although these Dirac points at the N point are energetically unfavorable, oxide heterostructures would offer an avenue for designing a Dirac metallic phase by tuning the Fermi level closer to these Dirac points by strain or chemical substitution.

The Fermi velocity and effective mass near the Dirac point were estimated to be 7.07×10^7 m/s and 0.026 m_e, respectively. The high Fermi velocity near the P point was also expected to give rise to a high carrier mobility in strained $SrNbO_3$ thin films.

Strain-tunable Dirac metallic state in $SrNbO_3$

As observed in our lattice symmetry measurements and octahedral rotation-induced half-order superstructure diffraction measurements, the substrate strain in the thin-film limit stabilized $SrNbO_3$ into a tetragonal crystalline symmetry (space group: *I4/mcm*) in which the NbO_6 octahedra were rotated only in the *x*-*y* plane along the *z* axis. As discussed in the main text, Dirac points appeared at the P point and at the N point of the Brillouin zone in this tetragonal crystalline environment. Figure S5 shows the band dispersions at three different levels of the octahedral rotation. The Dirac point at the P point is found to remain closer to the Fermi energy in all three cases. The three Dirac points at the N point come closer to the Fermi energy with increasing octahedral rotation, as shown in fig. S5 (D to F), enabling them to be available in the electronic transport. The octahedral rotation, therefore, offers a route to tune the Dirac points in a controlled manner that can be efficiently engineered in oxide heterostructures by using the substrate strain.

Transport measurements

Electrical transport measurements in this work were conducted with three measurement systems: the 14 T Physical Property Measurement System (Quantum Design), an 18 T dilution refrigerator at the University of Pittsburgh, and a 30 T bitter magnet with a He^3 cryostat at the National High Magnetic Field Laboratory (Tallahassee, USA). Results from different systems and different samples were reproducible and consistent. Aluminum wire-bonded contacts with a Van de Pauw configuration were used for measuring magnetotransport properties.

Strain-tunable multiband nature of $SrNbO_3$ thin films

Figure S6A shows the normalized Hall resistivity ρ_{xy} of $SrNbO_3$ thin films with different thicknesses. Although a fully relaxed thin film (d = 74 nm) shows linear Hall effects, nonlinear Hall effects were observed in the strained films ($d < d_{c1}$). To explain the observed nonlinear Hall effects in the $SrNbO_3$ thin films, a semiclassical two-band model was used

$$\rho_{xy} = \frac{\left(\mu_e^2 n_h + \mu_h^2 n_e\right) + (\mu_e \mu_h B)^2 (n_e + n_h)}{e\left[\mu_e |n_e| + \mu_h |n_h|\right)^2 + \left[\mu_e \mu_h (n_e + n_h) B\right]^2\right]} B$$

with the restriction of zero field resistivity

$$\rho_{xx}(0) = \frac{1}{e\left[\mu_e |n_e| + \mu_h |n_h|\right]}$$

where n_e(n_h) and μ_e(μ_h) are the carrier density and mobility, respectively, for electron(hole) type charge carriers. Figure S6B shows the magnetic field dependence of $\rho_{xy}(H)$ (black dots) with fitting curves (colored solid lines). The convex-shaped $\rho_{xy}(H)$ for a 6.4-nm thickness film was well explained by using two electron carriers, and the concave-shaped $\rho_{xy}(H)$ found in the 12.4-nm-thickness film was captured by electron and hole carriers.

Figure S7 shows the temperature dependence of the estimated mobility and carrier density for strained (d = 6.4 nm) and fully relaxed (d = 74 nm) $SrNbO_3$ thin films. The temperature dependence of the electron mobility for both samples shows typical behavior, which follows the Matthiessen rule: $\mu^{-1} = \mu_0^{-1} + \mu_{e-e}^{-1} + \mu_{LO}^{-1}$, where μ_0 describes the temperature-independent scattering from impurities or interface roughness that dominates at low temperature, $\mu_{e-e} \propto T^2$ quantifies the electron-electron scattering for intermediate temperatures,

and μ_{LO} is the highly temperature-dependent electron-phonon scattering term (*62*). The carrier densities of two different samples, however, show clearly different degrees of temperature dependence. Whereas the carrier density of the relaxed film does not change significantly, that of the strained film decreases by two orders of magnitude at low temperature. These observations further highlight the strain-induced electronic structure change. As explained earlier, two types of electrons contribute to the transport properties of the stained thin film: one with high mobility and low carrier density, and the other with low mobility and high carrier density. The former can be regarded as the origin of the quantum oscillation with the Dirac nature, as discussed in detail in the main text. The latter, however, may come from a simple parabolic band and may not be able to generate quantum oscillations because of a large scattering rate. Under such a multicarrier condition, the longitudinal and Hall conductivities can be estimated by the following equations

$$\sigma_{xx} = \sum \frac{n_i e \mu_i}{1 + (\mu_i B)^2} \text{ and } \sigma_{xy} = \sum \frac{n_i e \mu_i^2 B}{1 + (\mu_i B)^2}$$

Thus, the high-mobility electrons dominated the transport properties at low temperature, especially under magnetic fields. Thus, one of the carriers could reach the quantum limit, although strained $SrNbO_3$ has multiple carriers. The compounds $ZrTe_5$ and $HfTe_5$ are other good examples in which only one carrier among multiple carriers shows quantum limit behavior (*63*, *64*).

Aperiodic oscillations

Figure S8 (A and B) displays the low-temperature MR and Hall resistivity of different $SrNbO_3$ thin films with almost the same thickness, ~6.4 nm. All samples (S1 to S4) show consistent oscillations and the convex-shaped Hall effect that can be explained by the presence of two electron carriers, as previously discussed. Note that the oscillations are seen only in the films that have convex-shaped Hall effects. This finding supports the idea that one of the electron carriers, with low carrier density and high mobility, contributes to the oscillations. The oscillations are more pronounced in the second derivative curves ($-d^2\rho/dH^2$), as shown in fig. S8C. The minima of resistance are consistent with the minima of the second derivative, as displayed in fig. S9A.

By assigning the minima in oscillations to an integer Landau level index (N), we plotted the Landau fan diagram as illustrated in fig. S9C. The $1/H$ versus N deviates significantly from a conventional linear dependence. This unusual behavior cannot be explained even considering the strong Zeeman splitting with an enormous Lande g-factor. For the unconventional behavior to be explained as the effect of Zeeman splitting, at least the low–magnetic field region would have to show linear behavior, and its extrapolated line should be passing through near $N = 0$. However, we could not find any field region in which the Landau fan diagram showed liner behavior, even under a low magnetic field. Furthermore, the slope of the Landau fan diagram in a low–magnetic field region is too steep to pass $N = 0$. The deviation from conventional linear dependence is observed even in the low–magnetic field $H < 3$ T, at which the Zeeman effects are negligible (Zeeman energy < 0.5 meV). The unusual periodicity of oscillations, however, can be understood if the fractional Landau levels are taken into account, as discussed in the main text.

Note that aperiodic oscillations were also reported in $LaAlO_3/SrTiO_3$ samples. They were attributed to apparent spin degeneracy (*65*) and magnetic field–dependent electronic bands of titanium d_{yz}/d_{xz} orbitals (*66*). Both cases were based on the large effective mass of 1.4 to 1.7 m_e as experimentally confirmed. Unlike the behaviors of $LaAlO_3/SrTiO_3$ 2DEGs, the $SrNbO_3$ films had an extremely small effective mass and giant mass enhancement at high fields that cannot be explained by the scenarios used for $LaAlO_3/SrTiO_3$.

Strong mass enhancement at quantum limit

Figure S10 illustrates the magnetic field dependence of oscillations at different temperatures, showing their clear temperature and field dependence. With the temperature dependence of oscillations, the effective mass m^* can be estimated by using the Lifshitz-Kosevich formula $\Delta\rho_{xx} \propto (\alpha m^* T/H)/\sinh(\alpha m^* T/H)$, where $\alpha = 2\pi^2 ck_B \approx 14.69$ T/K. Figure S10A shows mass plots for oscillations under several magnetic fields. In conventional cases, the effective mass does not change as a function of magnetic field. However, the strong magnetic field dependence of the effective mass is clearly seen in strained $SrNbO_3$ films. The magnetic field dependence of the effective mass is summarized in Fig. 4.

Origin of transport properties

Although there was charge accumulation at the interface, the transport properties were dominated by the $SrNbO_3$ rather than by the interface. Figure S11 shows the carrier density dependence of mobility for the $SrNbO_3/SrTiO_3$ thin films and $SrTiO_3$-related materials (*67*). $SrNbO_3$ itself is the metal, with a huge number of carriers, $n \sim 10^{22}$ cm^{-3}, which is three to five orders of magnitude larger than the number in the 2DEG in $SrTiO_3$-related materials. Furthermore, the carriers with a larger density, $n \sim 10^{21}$ to 10^{22} cm^{-3}, in $SrNbO_3$ show one order of magnitude higher mobility than the 2DEG. The difference results from the effective mass difference between the two materials ($m^* \sim 0.1\ m_e$ for $SrNbO_3$ and $m^* \sim 1$ to 2 m_e for 2DEG in $SrTiO_3$). The transport properties observed in $SrNbO_3/SrTiO_3$, therefore, originated from the $SrNbO_3$ itself rather than from the interface, because of the larger carrier density and higher mobility of $SrNbO_3$.

In addition, the observed quantum oscillations were not related to the interfacial electrons for the following reasons. First, the effective mass estimated from quantum oscillation is too light to be explained with a 2DEG. The typical effective mass of a $SrTiO_3$-based 2DEG is ~1 to 2 m_e as found in $LaAlO_3/SrTiO_3$ (*68*), $Al_2O_3/SrTiO_3$ (*69*), and so on. Second, the quantum oscillation captures the 3D feature of the Fermi surface. The EELS spectrum directly verified that the excess electrons were mostly localized at the first monolayer of the substrate, which cannot account for the 3D Fermi surface. The 3D character can arise if the electron wavelength is smaller than the thickness. On the basis of the de Broglie relation, the electron wavelength is $\lambda = h/(m^* \cdot v)$. For a typical 2DEG in $SrTiO_3$, the wavelength is estimated to be ~0.7 nm ($v = 10^6$ m/s and $m^* = 1\ m_e$ for typical electrons). Thus, 1- to 2-unit cells of $SrTiO_3$ exhibit a 2D character ($\lambda \geq d$) as previously reported (*68*). On the other hand, metallic $SrNbO_3$ can have a 3D Fermi surface. By considering the Fermi velocity of $SrNbO_3$ near the Dirac point $v = 7.07 \times 10^7$ m/s, which is an order of magnitude higher than the typical electron velocity of 10^6 m/s, one can estimate the wavelengths of $SrNbO_3$ electrons. The wavelength of $SrNbO_3$ at a low field with $m^* \sim 0.1\ m_e$ is expected to be 0.1 nm (λ << thickness); thus, $SrNbO_3$ could give rise to a 3D feature.

SUPPLEMENTARY MATERIALS

Supplementary material for this article is available at https://science.org/doi/10.1126/sciadv.abf9631

REFERENCES AND NOTES

1. D. N. Basov, R. D. Averitt, D. Hsieh, Towards properties on demand in quantum materials. *Nat. Mater.* **16**, 1077–1088 (2017).
2. Y. Tokura, M. Kawasaki, N. Nagaosa, Emergent functions of quantum materials. *Nat. Phys.* **13**, 1056–1068 (2017).
3. B. Keimer, J. E. Moore, The physics of quantum materials. *Nat. Phys.* **13**, 1045–1055 (2017).
4. A. Banerjee, J. Yan, J. Knolle, C. A. Bridges, M. B. Stone, M. D. Lumsden, D. G. Mandrus, D. A. Tennant, R. Moessner, S. E. Nagler, Neutron scattering in the proximate quantum spin liquid α-$RuCl_3$. *Science* **356**, 1055–1059 (2017).
5. A. Banerjee, C. A. Bridges, J.-Q. Yan, A. A. Aczel, L. Li, M. B. Stone, G. E. Granroth, M. D. Lumsden, Y. Yiu, J. Knolle, S. Bhattacharjee, D. L. Kovrizhin, R. Moessner, D. A. Tennant, D. G. Mandrus, S. E. Nagler, Proximate Kitaev quantum spin liquid behaviour in a honeycomb magnet. *Nat. Mater.* **15**, 733–740 (2016).
6. S.-H. Do, S.-Y. Park, J. Yoshitake, J. Nasu, Y. Motome, Y. S. Kwon, D. T. Adroja, D. J. Voneshen, K. Kim, T.-H. Jang, J.-H. Park, K.-Y. Choi, S. Ji, Majorana fermions in the Kitaev quantum spin system α-$RuCl_3$. *Nat. Phys.* **13**, 1079–1084 (2017).
7. K. Matano, M. Kriener, K. Segawa, Y. Ando, G.-q. Zheng, Spin-rotation symmetry breaking in the superconducting state of $Cu_xBi_2Se_3$. *Nat. Phys.* **12**, 852–854 (2016).
8. Y. Li, X. Xu, M.-H. Lee, M.-W. Chu, C. L. Chien, Observation of half-quantum flux in the unconventional superconductor β-Bi_2Pd. *Science* **366**, 238–241 (2019).
9. C.-Z. Chang, J. Zhang, X. Feng, J. Shen, Z. Zhang, M. Guo, K. Li, Y. Ou, P. Wei, L.-L. Wang, Z.-Q. Ji, Y. Feng, S. Ji, X. Chen, J. Jia, X. Dai, Z. Fang, S.-C. Zhang, K. He, Y. Wang, L. Lu, X.-C. Ma, Q.-K. Xue, Experimental observation of the quantum anomalous Hall effect in a magnetic topological insulator. *Science* **340**, 167–170 (2013).
10. C.-Z. Chang, W. Zhao, D. Y. Kim, H. Zhang, B. A. Assaf, D. Heiman, S.-C. Zhang, C. Liu, M. H. W. Chan, J. S. Moodera, High-precision realization of robust quantum anomalous Hall state in a hard ferromagnetic topological insulator. *Nat. Mater.* **14**, 473–477 (2015).
11. K. I. Bolotin, F. Ghahari, M. D. Shulman, H. L. Stormer, P. Kim, Observation of the fractional quantum Hall effect in graphene. *Nature* **462**, 196–199 (2009).
12. D. C. Tsui, H. L. Stormer, A. C. Gossard, Two-dimensional magnetotransport in the extreme quantum limit. *Phys. Rev. Lett.* **48**, 1559–1562 (1982).
13. S. F. Nelson, K. Ismail, J. J. Nocera, F. F. Fang, E. E. Mendez, J. O. Chu, B. S. Meyerson, Observation of the fractional quantum Hall effect in Si/SiGe heterostructures. *Appl. Phys. Lett.* **61**, 64–66 (1992).
14. A. Tsukazaki, S. Akasaka, K. Nakahara, Y. Ohno, H. Ohno, D. Maryenko, A. Ohtomo, M. Kawasaki, Observation of the fractional quantum Hall effect in an oxide. *Nat. Mater.* **9**, 889–893 (2010).
15. J. G. Analytis, R. D. McDonald, S. C. Riggs, J.-H. Chu, G. S. Boebinger, I. R. Fisher, Two-dimensional surface state in the quantum limit of a topological insulator. *Nat. Phys.* **6**, 960–964 (2010).
16. W. Yu, Y. Jiang, J. Yang, Z. L. Dun, H. D. Zhou, Z. Jiang, P. Lu, W. Pan, Quantum oscillations at integer and fractional Landau level indices in single-crystalline $ZrTe_5$. *Sci. Rep.* **6**, 35357 (2016).
17. H. Wang, H. Liu, Y. Li, Y. Liu, J. Wang, J. Liu, J.-Y. Dai, Y. Wang, L. Li, J. Yan, D. Mandrus, X. C. Xie, J. Wang, Discovery of log-periodic oscillations in ultraquantum topological materials. *Sci. Adv.* **4**, eaau5096 (2018).
18. B. I. Halperin, Possible states for a three-dimensional electron gas in a strong magnetic field. *Jpn. J. Appl. Phys.* **26**, 1913–1919 (1987).
19. A. H. MacDonald, G. W. Bryant, Strong-magnetic-field states of the pure electron plasma. *Phys. Rev. Lett.* **58**, 515–518 (1987).
20. R. Willett, J. P. Eisenstein, H. L. Störmer, D. C. Tsui, A. C. Gossard, J. H. English, Observation of an even-denominator quantum number in the fractional quantum Hall effect. *Phys. Rev. Lett.* **59**, 1776–1779 (1987).
21. C. Nayak, S. H. Simon, A. Stern, M. Freedman, S. Das Sarma, Non-Abelian anyons and topological quantum computation. *Rev. Mod. Phys.* **80**, 1083–1159 (2008).
22. N. Samarth, Quantum materials discovery from a synthesis perspective. *Nat. Mater.* **16**, 1068–1076 (2017).
23. H. Boschker, J. Mannhart, Quantum-matter heterostructures. *Annu. Rev. Condens. Matter Phys.* **8**, 145–164 (2017).
24. A. K. Geim, I. V. Grigorieva, Van der Waals heterostructures. *Nature* **499**, 419–425 (2013).
25. C. N. R. Rao, Transition metal oxides. *Annu. Rev. Phys. Chem.* **40**, 291–326 (1989).
26. Y. Tokura, Correlated-electron physics in transition-metal oxides. *Phys. Today* **56**, 50–55 (2003).
27. J. Fujioka, R. Yamada, M. Kawamura, S. Sakai, M. Hirayama, R. Arita, T. Okawa, D. Hashizume, M. Hoshino, Y. Tokura, Strong-correlation induced high-mobility electrons in Dirac semimetal of perovskite oxide. *Nat. Commun.* **10**, 362 (2019).
28. J. Shiogai, T. Chida, K. Hashimoto, K. Fujiwara, T. Sasaki, A. Tsukazaki, Signature of band inversion in the perovskite thin-film alloys $BaSn_{1-x}Pb_xO_3$. *Phys. Rev. B* **101**, 125125 (2020).
29. Z. T. Liu, M. Y. Li, Q. F. Li, J. S. Liu, W. Li, H. F. Yang, Q. Yao, C. C. Fan, X. G. Wan, Z. Wang, D. W. Shen, Direct observation of the Dirac nodes lifting in semimetallic perovskite $SrIrO_3$ thin films. *Sci. Rep.* **6**, 30309 (2016).
30. K. Takiguchi, Y. K. Wakabayashi, H. Irie, Y. Krockenberger, T. Otsuka, H. Sawada, S. A. Nikolaev, H. Das, M. Tanaka, Y. Taniyasu, H. Yamamoto, Quantum transport evidence of Weyl fermions in an epitaxial ferromagnetic oxide. *Nat. Commun.* **11**, 4969 (2020).
31. T. Zhang, Y. Jiang, Z. Song, H. Huang, Y. He, Z. Fang, H. Weng, C. Fang, Catalogue of topological electronic materials. *Nature* **566**, 475–479 (2019).
32. T. Nan, T. J. Anderson, J. Gibbons, K. Hwang, N. Campbell, H. Zhou, Y. Q. Dong, G. Y. Kim, D. F. Shao, T. R. Paudel, N. Reynolds, X. J. Wang, N. X. Sun, E. Y. Tsymbal, S. Y. Choi, M. S. Rzchowski, Y. B. Kim, D. C. Ralph, C. B. Eom, Anisotropic spin-orbit torque generation in epitaxial $SrIrO_3$ by symmetry design. *Proc. Natl. Acad. Sci. U.S.A.* **116**, 16186–16191 (2019).
33. J. M. Rondinelli, S. J. May, J. W. Freeland, Control of octahedral connectivity in perovskite oxide heterostructures: An emerging route to multifunctional materials discovery. *MRS Bull.* **37**, 261–270 (2012).
34. T. C. Asmara, D. Wan, Y. Zhao, M. A. Majidi, C. T. Nelson, M. C. Scott, Y. Cai, B. Yan, D. Schmidt, M. Yang, T. Zhu, P. E. Trevisanutto, M. R. Motapothula, Y. P. Feng, M. B. H. Breese, M. Sherburne, M. Asta, A. Minor, T. Venkatesan, A. Rusydi, Tunable and low-loss correlated plasmons in Mott-like insulating oxides. *Nat. Commun.* **8**, 15271 (2017).
35. D. Oka, Y. Hirose, S. Nakao, T. Fukumura, T. Hasegawa, Intrinsic high electrical conductivity of stoichiometric $SrNbO_3$ epitaxial thin films. *Phys. Rev. B* **92**, 205102 (2015).
36. S. M. Young, C. L. Kane, Dirac semimetals in two dimensions. *Phys. Rev. Lett.* **115**, 126803 (2015).
37. M. L. Jin, F. Sun, L. Y. Xing, S. J. Zhang, S. M. Feng, P. P. Kong, W. M. Li, X. C. Wang, J. L. Zhu, Y. W. Long, H. Y. Bai, C. Z. Gu, R. C. Yu, W. G. Yang, G. Y. Shen, Y. S. Zhao, H. K. Mao, C. Q. Jin, Superconductivity bordering Rashba type topological transition. *Sci. Rep.* **7**, 39699 (2017).
38. Y. Liu, Y. J. Long, L. X. Zhao, S. M. Nie, S. J. Zhang, Y. X. Weng, M. L. Jin, W. M. Li, Q. Q. Liu, Y. W. Long, R. C. Yu, C. Z. Gu, F. Sun, W. G. Yang, H. K. Mao, X. L. Feng, Q. Li, W. T. Zheng, H. M. Weng, X. Dai, Z. Fang, G. F. Chen, C. Q. Jin, Superconductivity in $HfTe_5$ across weak to strong topological insulator transition induced via pressures. *Sci. Rep.* **7**, 44367 (2017).
39. F. Chen, J. Xia, D. K. Ferry, N. Tao, Dielectric screening enhanced performance in graphene FET. *Nano Lett.* **9**, 2571–2574 (2009).
40. J. S. Kim, S. S. A. Seo, M. F. Chisholm, R. K. Kremer, H.-U. Habermeier, B. Keimer, H. N. Lee, Nonlinear Hall effect and multichannel conduction in $LaTiO_3/SrTiO_3$ superlattices. *Phys. Rev. B* **82**, 201407(R) (2010).
41. O. N. Tufte, P. W. Chapman, Electron mobility in semiconducting strontium titanate. *Phys. Rev.* **155**, 796–802 (1967).
42. A. Bhattacharya, B. Skinner, G. Khalsa, A. V. Suslov, Spatially inhomogeneous electron state deep in the extreme quantum limit of strontium titanate. *Nat. Commun.* **7**, 12974 (2016).
43. A. A. Abrikosov, Galvanomagnetic phenomena in metals in quantum limit. *Sov. Phys. JETP* **29**, 746 (1969).
44. D.-X. Qu, Y. S. Hor, J. Xiong, R. J. Cava, N. P. Ong, Quantum oscillations and Hall anomaly of surface states in the topological insulator Bi_2Te_3. *Science* **329**, 821–824 (2010).
45. T. Liang, Q. Gibson, M. N. Ali, M. Liu, R. J. Cava, N. P. Ong, Ultrahigh mobility and giant magnetoresistance in the Dirac semimetal Cd_3As_2. *Nat. Mater.* **14**, 280–284 (2015).
46. K. Wang, D. Graf, H. Lei, S. W. Tozer, C. Petrovic, Quantum transport of two-dimensional Dirac fermions in $SrMnBi_2$. *Phys. Rev. B* **84**, 220401(R) (2011).
47. M. J. Veit, R. Arras, B. J. Ramshaw, R. Pentcheva, Y. Suzuki, Nonzero Berry phase in quantum oscillations from giant Rashba-type spin splitting in $LaTiO_3/SrTiO_3$ heterostructures. *Nat. Commun.* **9**, 1458 (2018).
48. P. Noël, F. Trier, L. M. Vicente Arche, J. Bréhin, D. C. Vaz, V. Garcia, S. Fusil, A. Barthélémy, L. Vila, M. Bibes, J.-P. Attané, Non-volatile electric control of spin-charge conversion in a $SrTiO_3$ Rashba system. *Nature* **580**, 483–486 (2020).
49. P. T. Coleridge, Z. W. Wasilewski, P. Zawadzki, A. S. Sachrajda, H. A. Carmona, Composite-fermion effective masses. *Phys. Rev. B* **52**, R11603(R) (1995).
50. S. Pezzini, M. R. van Delft, L. M. Schoop, B. V. Lotsch, A. Carrington, M. I. Katsnelson, N. E. Hussey, S. Wiedmann, Unconventional mass enhancement around the Dirac nodal loop in ZrSiS. *Nat. Phys.* **14**, 178–183 (2018).
51. A. Ohtomo, D. A. Muller, J. L. Grazul, H. Y. Hwang, Epitaxial growth and electronic structure of $LaTiO_x$ films. *Appl. Phys. Lett.* **80**, 3922–3924 (2002).
52. W. S. Choi, S. A. Lee, J. H. You, S. Lee, H. N. Lee, Resonant tunnelling in a quantum oxide superlattice. *Nature Commun.* **6**, 7424 (2015).
53. G.-z. Zhu, G. Radtke, G. A. Botton, Bonding and structure of a reconstructed (001) surface of $SrTiO_3$ from TEM. *Nature* **490**, 384–387 (2012).
54. H. N. Lee, S. S. A. Seo, W. S. Choi, C. M. Rouleau, Growth control of oxygen stoichiometry in homoepitaxial $SrTiO_3$ films by pulsed laser epitaxy in high vacuum. *Sci. Rep.* **6**, 19941 (2016).
55. Z. Zhong, P. Hansmann, Band alignment and charge transfer in complex oxide interfaces. *Phys. Rev. X* **7**, 011023 (2017).

56. G. Khalsa, A. H. MacDonald, Theory of the $SrTiO_3$ surface state two-dimensional electron gas. *Phys. Rev. B* **86**, 125121 (2012).
57. Z. Zhong, P. Wissgott, K. Held, G. Sangiovanni, Microscopic understanding of the orbital splitting and its tuning at oxide interfaces. *Europhys. Lett.* **99**, 37011 (2012).
58. J. P. Perdew, K. Burke, M. Ernzerhof, Generalized gradient approximation made simple. *Phys. Rev. Lett.* **77**, 3865–3868 (1996).
59. P. Giannozzi, S. Baroni, N. Bonini, M. Calandra, R. Car, C. Cavazzoni, D. Ceresoli, G. L. Chiarotti, M. Cococcioni, I. Dabo, A. D. Corso, S. de Gironcoli, S. Fabris, G. Fratesi, R. Gebauer, U. Gerstmann, C. Gougoussis, A. Kokalj, M. Lazzeri, L. Martin-Samos, N. Marzari, F. Mauri, R. Mazzarello, S. Paolini, A. Pasquarello, L. Paulatto, C. Sbraccia, S. Scandolo, G. Sclauzero, A. P. Seitsonen, A. Smogunov, P. Umari, R. M. Wentzcovitch, QUANTUM ESPRESSO: A modular and open-source software project for quantum simulations of materials. *J. Phys. Condens. Matter* **21**, 395502 (2009).
60. C. Bigi, P. Orgiani, J. Sławińska, J. Fujii, J. T. Irvine, S. Picozzi, G. Panaccione, I. Vobornik, G. Rossi, D. Payne, F. Borgatti, Direct insight into the band structure of $SrNbO_3$. *Phys. Rev. Mater.* **4**, 025006 (2020).
61. Y. Park, J. Roth, D. Oka, Y. Hirose, T. Hasegawa, A. Paul, A. Pogrebnyakov, V. Gopalan, T. Birol, R. Engel-Herber, $SrNbO_3$ as a transparent conductor in the visible and ultraviolet spectra. *Commun. Phys.* **3**, 102 (2020).
62. E. Mikheev, B. Himmetoglu, A. P. Kajdos, P. Moetakef, T. A. Cain, C. G. Van de Walle, S. Stemmer, Limitations to the room temperature mobility of two- and three-dimensional electron liquids in $SrTiO_3$. *Appl. Phys. Lett.* **106**, 062102 (2015).
63. Y. Liu, X. Yuan, C. Zhang, Z. Jin, A. Narayan, C. Luo, Z. Chen, L. Yang, J. Zou, X. Wu, S. Sanvito, Z. Xia, L. Li, Z. Wang, F. Xiu, Zeeman splitting and dynamical mass generation in Dirac semimetal $ZrTe_5$. *Nat. Commun.* **7**, 12516 (2016).
64. P. Wang, Y. Ren, F. Tang, P. Wang, T. Hou, H. Zeng, L. Zhang, Z. Qiao, Approaching three-dimensional quantum Hall effect in bulk $HfTe_5$. *Phys. Rev. B* **101**, 161201(R) (2020).
65. F. Trier, G. E. D. K. Prawiroatmodjo, Z. Zhong, D. V. Christensen, M. von Soosten, A. Bhowmik, J. M. G. Lastra, Y. Chen, T. S. Jespersen, N. Pryds, Quantization of Hall resistance at the metallic interface between an oxide insulator and $SrTiO_3$. *Phys. Rev. Lett.* **117**, 096804 (2016).
66. K. Rubi, J. Gosteau, R. Serra, K. Han, S. Zeng, Z. Huang, B. Warot-Fonrose, R. Arras, E. Snoeck, Ariando, M. Goiran, W. Escoffier, Aperiodic quantum oscillations in the two-dimensional electron gas at the $LaAlO_3/SrTiO_3$ interface. *npj Quantum Mater.* **5**, 9 (2020).
67. F. Trier, K. V. Reich, D. V. Christensen, Y. Zhang, H. L. Tuller, Y. Chen, B. I. Shklovskii, N. Pryds, Universality of electron mobility in $LaAlO_3/SrTiO_3$ and bulk $SrTiO_3$. *Appl. Phys. Lett.* **111**, 092106 (2017).
68. A. D. Caviglia, S. Gariglio, C. Cancellieri, B. Sacépé, A. Fête, N. Reyren, M. Gabay, A. F. Morpurgo, J.-M. Triscone, Two-dimensional quantum oscillations of the conductance at $LaAlO_3/SrTiO_3$ interfaces. *Phys. Rev. Lett.* **105**, 236802 (2010).
69. Y. Z. Chen, N. Bovet, F. Trier, D. V. Christensen, F. M. Qu, N. H. Andersen, T. Kasama, W. Zhang, R. Giraud, J. Dufouleur, T. S. Jespersen, J. R. Sun, A. Smith, J. Nygård, L. Lu, B. Büchner, B. G. Shen, S. Linderoth, N. Pryds, A high-mobility two-dimensional electron gas at the spinel/perovskite interface of γ-$Al_2O_3/SrTiO_3$. *Nat. Commun.* **4**, 1371 (2013).
70. H. P. R. Frederikse, W. R. Hosler, W. R. Thurber, J. Babiskin, P. G. Siebenmann, Shubnikov-de Haas effect in $SrTiO_3$. *Phys. Rev.* **158**, 775–778 (1967).
71. X. Lin, Z. Zhu, B. Fauqué, K. Behnia, Fermi surface of the most dilute superconductor. *Phys. Rev. X* **3**, 021002 (2013).
72. Y. Kozuka, M. Kim, C. Bell, B. G. Kim, Y. Hikita, H. Y. Hwang, Two-dimensional normal-state quantum oscillations in a superconducting heterostructure. *Nature* **462**, 487–490 (2009).
73. M. Kim, C. Bell, Y. Kozuka, M. Kurita, Y. Hikita, H. Y. Hwang, Fermi surface and superconductivity in low-density high-mobility δ-doped $SrTiO_3$. *Phys. Rev. Lett.* **107**, 106801 (2011).
74. A. P. Kajdos, D. G. Ouellette, T. A. Cain, S. Stemmer, Two-dimensional electron gas in a modulation-doped $SrTiO_3/Sr(Ti, Zr)O_3$ heterostructure. *Appl. Phys. Lett.* **103**, 082120 (2013).
75. P. Moetakef, D. G. Ouellette, J. R. Williams, S. J. Allen, L. Balents, D. Goldhaber-Gordon, S. Stemmer, Quantum oscillations from a two-dimensional electron gas at a Mott/band insulator interface. *Appl. Phys. Lett.* **101**, 151604 (2012).
76. A. McCollam, S. Wenderich, M. K. Kruize, V. K. Guduru, H. J. A. Molegraaf, M. Huijben, G. Koster, D. H. A. Blank, G. Rijnders, A. Brinkman, H. Hilgenkamp, U. Zeitler, J. C. Maan, Quantum oscillations and subband properties of the two-dimensional electron gas at the $LaAlO_3/SrTiO_3$ interface. *APL Mater.* **2**, 022102 (2014).
77. M. J. Veit, M. K. Chan, B. J. Ramshaw, R. Arras, R. Pentcheva, Y. Suzuki, Three-dimensional character of the Fermi surface in ultrathin $LaTiO_3/SrTiO_3$ heterostructures. *Phys. Rev. B* **99**, 115126 (2019).
78. N. Kumar, N. Wadehra, R. Tomar, Shama, S. Kumar, Y. Singh, S. Dattagupta, S. Chakraverty, Observation of Shubnikov-de Haas oscillations, planar Hall effect, and anisotropic magnetoresistance at the conducting interface of $EuO-KTaO_3$. *Adv. Quantum Technol.* **4**, 2000081 (2021).

Acknowledgments: We thank J. S. Kim, Y. Kim, and M. Brahlek for discussion. **Funding:** This work was supported by the U.S. Department of Energy (DOE), Office of Science, Basic Energy Sciences, Materials Sciences and Engineering Division, and in part by the Computational Materials Sciences Program. The high–magnetic field measurements were performed at the National High Magnetic Field Laboratory, which is supported by NSF cooperative agreement no. DMR-1644779 and the state of Florida. This research used resources of the Advanced Photon Source, a DOE Office of Science User Facility, operated for the DOE Office of Science by Argonne National Laboratory under contract no. DE-AC02-06CH11357. Extraordinary facility operations were supported, in part, by the DOE Office of Science through the National Virtual Biotechnology Laboratory, a consortium of DOE national laboratories focused on the response to COVID-19, with funding provided by the Coronavirus CARES Act. W.S.C. was supported by Basic Science Research Programs through the National Research Foundation of Korea (NRF) (NRF-2021R1A2C2011340). J.L. acknowledges support from NSF (PHY-1913034) and Vannevar Bush Faculty Fellowship (N00014-15-1-2847). **Author contributions:** J.M.O. and H.N.L. conceived the project. J.M.O. and J.Z. grew films and conducted characterization with help from E.S., C.S., H.L., H.M., W.S.C., and G.E. N.M. and S.O. performed DFT calculations. S.Y. and A.R.L. conducted STEM experiments. H.Z. conducted synchrotron XRD measurements. J.M.O. performed transport measurements with help from J.Z., E.S.C., Y.-Y.P., B.L., M.B., P.I., and J.L. J.M.O. and H.N.L. wrote the manuscript with input from all authors. **Competing interests:** The authors declare that they have no competing interests. **Data and materials availability:** All data needed to evaluate the conclusions in the paper are present in the paper and/or the Supplementary Materials.

Submitted 1 December 2020
Accepted 23 July 2021
Published 15 September 2021
10.1126/sciadv.abf9631

Citation: J. M. Ok, N. Mohanta, J. Zhang, S. Yoon, S. Okamoto, E. S. Choi, H. Zhou, M. Briggeman, P. Irvin, A. R. Lupini, Y.-Y. Pai, E. Skoropata, C. Sohn, H. Li, H. Miao, B. Lawrie, W. S. Choi, G. Eres, J. Levy, H. N. Lee, Correlated oxide Dirac semimetal in the extreme quantum limit. *Sci. Adv.* **7**, eabf9631 (2021).

ScienceAdvances

Correlated oxide Dirac semimetal in the extreme quantum limit

Jong Mok OkNarayan MohantaJie ZhangSangmoon YoonSatoshi OkamotoEun Sang ChoiHua ZhouMegan BriggemanPatrick IrvinAndrew R. LupiniYun-Yi PaiElizabeth SkoropataChanghee SohnHaoxiang LiHu MiaoBenjamin LawrieWoo Seok ChoiGyula EresJeremy LevyHo Nyung Lee

Sci. Adv., 7 (38), eabf9631. • DOI: 10.1126/sciadv.abf9631

Science Advances (ISSN) is published by the American Association for the Advancement of Science. 1200 New York Avenue NW, Washington, DC 20005. The title *Science Advances* is a registered trademark of AAAS.